IMPLICIT-EXPLICIT INTEGRATION OF GRADIENT ENHANCED DAMAGE MODELS

Thomas Titscher[1], Javier Oliver[2], and Jörg F. Unger[3]

[1]Federal Institute for Materials Research and Testing (BAM), Unter den Eichen 87, 12205 Berlin, Germany, Email: thomas.titscher@bam.de

[2]Technical University of Catalonia (BarcelonaTech), International Center for Numerical Methods in Engineering (CIMNE), Campus Nord U.P.C., Edifici C-1, Jordi Girona 1-3, 08034 Barcelona, Spain

[3]Federal Institute for Materials Research and Testing (BAM), Unter den Eichen 87, 12205 Berlin, Germany, Email: joerg.unger@bam.de

Abstract

Quasi-brittle materials exhibit strain softening. Their modeling requires regularized constitutive formulations to avoid instabilities on the material level. A commonly used model is the implicit gradient enhanced damage model. For complex geometries, it still shows structural instabilities when integrated with classical backward Euler schemes. An alternative is the implicit-explicit (IMPL-EX) integration scheme. It consists of the extrapolation of internal variables followed by an implicit calculation of the solution fields. The solution procedure for the nonlinear gradient enhanced damage model is thus transformed into a sequence of problems that are algorithmically linear in every time step. Therefore, they require one single Newton-Raphson iteration per time step to converge. This provides both additional robustness and computational speedup. The introduced extrapolation error is controlled by adaptive time stepping schemes. Two novel classes of error control schemes that provide further performance improvements are introduced and assessed. In a three dimensional com-

pression test for a mesoscale model of concrete, the presented scheme provides a speedup of about 40 compared to an adaptive backward Euler time integration.

Keywords: implicit explicit schemes, gradient enhanced damage model, adaptive time stepping, continuum damage, robustness

INTRODUCTION

The implicit gradient enhanced damage formulation as introduced by (Peerlings et al. 1996) models quasi-brittle material failure. As opposed to the spontaneous failure of brittle materials, these materials exhibit strain softening. After reaching a peak load, quasi-brittle materials do not collapse instantly. Material defects like microcracks cause a loss of the material's stiffness. The load-carrying capacity gradually decreases for increasing deformations and complete material failure only occurs as soon as many microscopic defects connect to form a macroscopic crack.

In continuum damage mechanics, the loss of material stiffness is often modeled with a damage variable. Strain concentrations lead to material deterioration which itself causes strain growth. This process builds up to narrow localization bands and causes, without further treatment, various numerical problems.

In classical *local* continuum damage models, this band comprises only a single layer of elements. The local stress-strain relation has to include the element length (Oliver 1989) as an additional parameter to provide a regularized energy dissipation upon mesh refinement (Bažant and Belytschko 1985). This leads to smeared crack models with weak discontinuities (Rots et al. 1985; Jirásek and Zimmermann 1998; Carol and Bazant 1997). Alternatively, the location of the band can be predefined, e.g. in traction-separation interface models (Carol et al. 1997) or in the context of the continuum strong discontinuity framework (Oliver et al. 2002; Cazes et al. 2016).

Numerical problems arise in the backward Euler solution of local damage models. The acoustic tensor can become ill-conditioned (Jirásek 2007). This can lead to zero eigenvalues in the element stiffness matrices that propagate through the mesh eventually resulting in an ill-conditioned global algorithmic stiffness matrix (Oliver et al. 2006).

This issue can be solved by secant stiffness based methods. For each load step, the sequentially linear approach (Rots et al. 2008; Graça-e Costa et al. 2012) repeatedly identifies critical elements and adapts their internal variables until equilibrium is reached. The method can be applied to smeared and discrete crack models and exhibits a "saw tooth" load-displacement relation. An alternative is the implicit-explicit (IMPL-EX) scheme (Oliver et al. 2008) that is investigated in this paper. It adapts the internal variables in all elements simultaneously once per load step to obtain the secant stiffness. This requires only minor changes to existing model implementations and smoothly approximates the load-displacement curve.

Another type of model is a nonlocal models (Bažant and Jirásek 2002), either of the integral type (Bažant et al. 1984; Bazant and Pijaudier-Cabot 1988; De Vree et al. 1995) or in a gradient formulation (Triantafyllidis and Aifantis 1986; Pham et al. 2011). The focus of this paper is the implicit gradient enhanced damage model by (Peerlings et al. 1996) where the acoustic tensor is proven to remain well-posed (Peerlings et al. 1998). The damage variable is driven by a nonlocal equivalent strain field. Its evolution is described by an additional screened Poisson equation, which essentially limits the curvature of the nonlocal strain. This results in a smooth damage field. The fully damaged material in the center of a damage zone represents a macroscopic crack, the surrounding partially damage material represents a distribution of micro cracks.

When modeling complex geometries like concrete on the mesoscale - including aggregates, matrix material and interfaces (Unger and Eckardt 2011) - the number of structural instabilities increase. Accurately resolving the equilibrium path in a backward Euler scheme now requires tiny time steps and the computational cost increases. Here, the IMPL-EX scheme provides two benefits. First, its implementation of the method itself is less invasive and even the implementation of the mechanical models is simplified, because certain derivatives vanish. Secondly, it reduces the computational effort by improving the properties of the global matrix and by reducing the number of time steps required to finish the simulation.

The latter is achieved by using error control schemes (Oliver et al. 2008; Blanco et al. 2007). Each IMPL-EX iteration introduces an extrapolation error that depends on the time step length. The right choice of this time step ensures that the extrapolation error is limited to a prescribed value.

In this paper, the governing equations and the finite element discretization of the implicit gradient enhanced damage model are shown first, including the adaptive backward Euler scheme. Next, the IMPL-EX scheme and its application to the model are discussed in detail. A special focus is given to the development of a new class of adaptive time stepping schemes. The model is validated for a double-notched tensile test and the novel time stepping schemes are assessed. Two and three dimensional compression tests explore the potential speedup of the IMPL-EX method.

GOVERNING EQUATIONS

The thermodynamically consistent formulation of the implicit gradient enhanced damage model is derived in detail by (Peerlings et al. 2004) and briefly sketched here. In a simplified version, it resembles the original model introduced in (Peerlings et al. 1996).

The free energy potential ψ for the isothermal, linear elasticity deformation is postulated to be

$$\psi(\boldsymbol{\varepsilon}, \bar{\varepsilon}_{\mathrm{eq}}, \omega) = \frac{1}{2}(1-\omega)\boldsymbol{\varepsilon} : \boldsymbol{C} : \boldsymbol{\varepsilon} + \frac{1}{2}h(\varepsilon_{\mathrm{eq}} - \bar{\varepsilon}_{\mathrm{eq}})^2 + \frac{1}{2}hl^2\nabla\bar{\varepsilon}_{\mathrm{eq}} \cdot \nabla\bar{\varepsilon}_{\mathrm{eq}}. \tag{1}$$

The first term is the elastic potential, modified by the isotropic damage variable ω. Here, $\boldsymbol{\varepsilon}$ denotes the symmetric gradient of the displacement field $\boldsymbol{d}$ and $\boldsymbol{C}$ is the undamaged elasticity tensor. The second term describes the stored energy between a nonlocal strain field $\bar{\varepsilon}_{\mathrm{eq}}$ and a local strain norm $\varepsilon_{\mathrm{eq}}$. The latter one is defined as an invariant of the strain field $\boldsymbol{\varepsilon}$. The parameter h can be interpreted as a local-to-nonlocal coupling modulus. The third term includes the energy of gradients of the nonlocal strain field and the nonlocal length parameter l.

(Poh and Sun 2017) enhance this formulation based on the following idea. At the onset of damage, the nonlocal interaction causes the formation of diffuse networks of microcracks. As the load increases, the process zone width decreases and the elastic bulk material unloads. Towards material failure, a very narrow macroscopic crack forms. This is modeled with a decreasing nonlocal interaction function $g(\omega)$ that reduces the nonlocal length parameter upon damage growth. The enhanced free energy potential now reads

$$\psi(\boldsymbol{\varepsilon}, \bar{\varepsilon}_{\mathrm{eq}}, \omega) = \frac{1}{2}(1-\omega)\varepsilon : \boldsymbol{C} : \varepsilon + \frac{1}{2}h(\varepsilon_{\mathrm{eq}} - \bar{\varepsilon}_{\mathrm{eq}})^2 + \frac{1}{2}h\ g(\omega)\ l^2 \nabla\bar{\varepsilon}_{\mathrm{eq}} \cdot \nabla\bar{\varepsilon}_{\mathrm{eq}} \tag{2}$$

with

$$g(\omega) = \frac{(1-R)\exp(-\eta\omega) + R - \exp(-\eta)}{1 - \exp(-\eta)} \tag{3}$$

such that $g(\omega = 0) = 1$ and $g(\omega = 1) = R$, with the parameters $R = 0.005$ and $\eta = 5$. For thermodynamic consistency, the dissipation inequality

$$\dot{D} = \int_V \left[\boldsymbol{\sigma} : \dot{\boldsymbol{\varepsilon}} - \dot{\psi}\right] \mathrm{d}V \geq 0 \tag{4}$$

must be satisfied within the whole body volume V, where $\boldsymbol{\sigma}$ denotes the Cauchy stress and $\dot{(\ )}$ is the derivative of $(\ )$ with respect to time. Inserting the time derivative of Eq. (2) into Eq. (4) and integrating by parts yields

$$\begin{aligned}\dot{D} = &\int_V \left(\boldsymbol{\sigma} - (1-\omega)\boldsymbol{C} : \boldsymbol{\varepsilon} - h(\varepsilon_{\mathrm{eq}} - \bar{\varepsilon}_{\mathrm{eq}})\frac{\partial\varepsilon_{\mathrm{eq}}}{\partial\boldsymbol{\varepsilon}}\right) : \dot{\boldsymbol{\varepsilon}}\mathrm{d}V \\ &+ \int_V h\left[\varepsilon_{\mathrm{eq}} - \bar{\varepsilon}_{\mathrm{eq}} + g\ l^2\nabla^2\bar{\varepsilon}_{\mathrm{eq}}\right]\dot{\varepsilon}_{\mathrm{eq}}\mathrm{d}V - \int_S h\ g\ l^2\nabla\bar{\varepsilon}_{\mathrm{eq}} \cdot \boldsymbol{n}\dot{\varepsilon}_{\mathrm{eq}}\mathrm{d}S \\ &+ \int_V \left[\frac{1}{2}\boldsymbol{\varepsilon} : \boldsymbol{C} : \boldsymbol{\varepsilon} - \frac{1}{2}h\frac{\mathrm{d}g}{\mathrm{d}\omega}l^2\nabla^2\bar{\varepsilon}_{\mathrm{eq}}\right]\dot{\omega}\mathrm{d}V \geq 0.\end{aligned} \tag{5}$$

where S is the boundary of V with the outwards normal vector $\boldsymbol{n}$.

The stress-strain relation

$$\boldsymbol{\sigma} = (1 - \omega)\boldsymbol{C} : \boldsymbol{\varepsilon} + h(\varepsilon_{\text{eq}} - \bar{\varepsilon}_{\text{eq}})\frac{\partial \varepsilon_{\text{eq}}}{\partial \boldsymbol{\varepsilon}} \tag{6}$$

causes the first term of Eq. (5) to vanish.

We now require $\dot{D} = 0$ in the elastic regime ($\dot{\omega} = 0$) by fullfilling

$$\bar{\varepsilon}_{\text{eq}} - g l^2 \nabla^2 \bar{\varepsilon}_{\text{eq}} = \varepsilon_{\text{eq}} \text{ in } V \text{ and} \tag{7}$$

$$\nabla \bar{\varepsilon}_{\text{eq}} \cdot \boldsymbol{n} = 0 \text{ on } S. \tag{8}$$

The screened Poisson equation in Eq. (7) limits the curvature of the nonlocal equivalent strain field $\bar{\varepsilon}_{\text{eq}}$. Note that this equation (for $g \equiv 1$) can also be derived from a Taylor expansion of a nonlocal integral model (e.g. (Pijaudier-Cabot and Bažant 1987; Bazant and Pijaudier-Cabot 1988)) (Peerlings et al. 1996). In fact, it is equivalent to a nonlocal integral model with the Green's function of Eq. (7) as the weighting function (Peerlings et al. 2001). With Eqs. (6) to (8), the dissipation inequality from Eq. (5) now reads

$$\dot{D} = \int_V \left[\frac{1}{2}\boldsymbol{\varepsilon} : \boldsymbol{C} : \boldsymbol{\varepsilon} - \frac{1}{2} h \frac{\mathrm{d}g}{\mathrm{d}\omega} l^2 \nabla^2 \bar{\varepsilon}_{\text{eq}}\right] \dot{\omega} \mathrm{d}V \geq 0. \tag{9}$$

Since g is a monotonically decreasing function, the integrand remains non-negative as long as the damage growth remains non-negative. Therefore, damage is defined as a monotonically increasing function of the scalar history variable κ, which itself is driven by the nonlocal equivalent strains through the Karush–Kuhn–Tucker conditions

$$\dot{\kappa} \geq 0, \quad \bar{\varepsilon}_{\text{eq}} - \kappa \leq 0, \quad \dot{\kappa}(\bar{\varepsilon}_{\text{eq}} - \kappa) = 0. \tag{10}$$

A discretization in time steps Δt at time t leads to

$$\kappa_{t+\Delta t} = \max(\kappa_t, \bar{\varepsilon}_{\mathrm{eq},t+\Delta t}) \tag{11}$$

and points out the physical meaning. The history variable κ represents the highest nonlocal equivalent strain ever reached during the loading history.

The isotropic, exponential damage law $\omega(\kappa)$, (e.g. (Mazars and Pijaudier-Cabot 1989; Oliver et al. 1990; Peerlings et al. 1998)) is used for all numerical examples in this work.

$$\omega = \begin{cases} 0 & \text{if } \kappa < \kappa_0, \\ 1 - \frac{\kappa_0}{\kappa}\left(1 - \alpha + \alpha \exp\left(\beta(\kappa_0 - \kappa)\right)\right) & \text{otherwise,} \end{cases} \tag{12}$$

κ_0 is a damage initiation threshold, β controls the post peak slope and α ensures a residual strength. Inserted in Eq. (6) (with $h = 0$) and uniaxially loaded with $\varepsilon_x = \kappa$, a physical interpretation of these parameters is derived by

$$f_t = \max_{\kappa} \sigma_x, = \sigma_x(\kappa_0) = E\kappa_0, \tag{13}$$

$$f_{\mathrm{residual}} = \sigma_x(\kappa \to \infty) = (1 - \alpha) f_t \text{ and} \tag{14}$$

$$g_f = \int_{\kappa_0}^{\infty} \sigma_x(\kappa)\mathrm{d}\kappa = \frac{f_t}{\beta} \tag{15}$$

with the tensile strength f_t, the residual strength f_{residual} and the local fracture energy parameter g_f ([N/mm^2]). Note that the latter one does not correspond to the global fracture energy G_f ([N/mm]) obtained from experiments and has to be calibrated.

The different material behavior in tension and compression that quasi-brittle materials like concrete typically exhibit is accounted for in the definition of $\varepsilon_{\mathrm{eq}}$. The strain-based modified von Mises definition (De Vree et al. 1995) is employed, resulting in

$$\varepsilon_{\text{eq}}(\boldsymbol{\varepsilon}) = \frac{k-1}{2k(1-2\nu)} I_1 + \frac{1}{2k}\sqrt{\left(\frac{k-1}{1-2\nu} I_1\right)^2 + \frac{2k}{(1+\nu)^2} J_2} \tag{16}$$

with the first strain tensor invariant I_1, the second deviatoric strain invariant J_2 and Poisson's ratio ν. The factor $k = f_c/f_t$ expresses the ratio of the materials compressive strength f_c and its tensile strength f_t - a uniaxial tensile strain and a k-times higher uniaxial compressive strain both lead to the same ε_{eq}.

For the discretization of the full model, we refer to (Poh and Sun 2017). In this paper, a simplified version of the model with $h = 0$ is used, which is also thermodynamically admissible (Peerlings et al. 2004) Since the discretization offers insights on the IMPL-EX benefits, a brief introduction is given.

The nodal degrees of freedom are the displacements $\underline{\boldsymbol{d}}$ and the nonlocal equivalent strains $\underline{\bar{\boldsymbol{\varepsilon}}}_{\text{eq}}$. They are interpolated with the shape functions $\boldsymbol{N}$ and the derivative of the shape functions $\boldsymbol{B}$ such that the continuous fields $\boldsymbol{d}$ and $\bar{\varepsilon}_{\text{eq}}$ and their derivatives are approximated by

$$\boldsymbol{d} = \boldsymbol{N}\underline{\boldsymbol{d}}, \qquad \boldsymbol{\varepsilon} = \boldsymbol{B}\underline{\boldsymbol{d}}, \tag{17}$$

$$\bar{\varepsilon}_{\text{eq}} = \bar{\boldsymbol{N}}\underline{\bar{\boldsymbol{\varepsilon}}}_{\text{eq}} \text{ and } \qquad \nabla\bar{\varepsilon}_{\text{eq}} = \bar{\boldsymbol{B}}\underline{\bar{\boldsymbol{\varepsilon}}}_{\text{eq}}, \tag{18}$$

where $(\bar{\ })$ denotes the interpolation for the nonlocal equivalent strain field. The interpolations can be chosen independently for each degree of freedom type. As discussed in Appendix I, the highest order of convergence is obtained for identical interpolation orders. The discretized weak forms of local momentum balance $\nabla \cdot \boldsymbol{\sigma} = \boldsymbol{0}$ and the screened Poisson equation in

Eq. (7) are combined into a joint residual vector $\boldsymbol{R}$

$$\boldsymbol{R} = \begin{pmatrix} \boldsymbol{R}^d \\ \boldsymbol{R}^\varepsilon \end{pmatrix} = \boldsymbol{0} \text{ with} \tag{19}$$

$$\boldsymbol{R}^d = \int_\Omega \boldsymbol{B}^T (1-\omega) \boldsymbol{C} \boldsymbol{\varepsilon} \ \mathrm{d}\Omega \text{ and} \tag{20}$$

$$\boldsymbol{R}^\varepsilon = \int_\Omega \bar{\boldsymbol{N}}^T \left(\bar{\varepsilon}_{\mathrm{eq}} - \varepsilon_{\mathrm{eq}}\right) \ \mathrm{d}\Omega + \int_\Omega \bar{\boldsymbol{B}}^T g l^2 \nabla \bar{\varepsilon}_{\mathrm{eq}} \ \mathrm{d}\Omega \ . \tag{21}$$

BACKWARD EULER TIME INTEGRATION

The quasi-static problem is discretized into pseudo time steps Δt and the load is applied as a linear function of the pseudo time t until $t_{\mathrm{max}} = 1\,\mathrm{s}$. Equilibrium is obtained after load incrementation with Newton-Raphson iterations. The linear Taylor expansion leads to the system of equations

$$-\begin{bmatrix} \boldsymbol{K}^{dd} & \boldsymbol{K}^{d\varepsilon} \\ \boldsymbol{K}^{\varepsilon d} & \boldsymbol{K}^{\varepsilon\varepsilon} \end{bmatrix} \begin{pmatrix} \Delta \underline{\boldsymbol{d}} \\ \Delta \underline{\bar{\boldsymbol{\varepsilon}}}_{\mathrm{eq}} \end{pmatrix} = \begin{pmatrix} \boldsymbol{R}^d \\ \boldsymbol{R}^\varepsilon \end{pmatrix} \tag{22}$$

with

$$\boldsymbol{K}^{dd} = \frac{\partial \boldsymbol{R}^d}{\partial \boldsymbol{d}} = \int_\Omega (1-\omega) \boldsymbol{B}^T \boldsymbol{C} \boldsymbol{B} \ \mathrm{d}\Omega \tag{23}$$

$$\boldsymbol{K}^{d\varepsilon} = \frac{\partial \boldsymbol{R}^d}{\partial \bar{\varepsilon}_{\mathrm{eq}}} = -\int_\Omega \boldsymbol{B}^T \frac{\mathrm{d}\omega}{\mathrm{d}\kappa} \frac{\mathrm{d}\kappa}{\mathrm{d}\bar{\varepsilon}_{\mathrm{eq}}} \boldsymbol{C} \boldsymbol{\varepsilon} \bar{\boldsymbol{N}} \ \mathrm{d}\Omega \tag{24}$$

$$\boldsymbol{K}^{\varepsilon d} = \frac{\partial \boldsymbol{R}^\varepsilon}{\partial \boldsymbol{d}} = -\int_\Omega \bar{\boldsymbol{N}}^T \frac{\partial \varepsilon_{\mathrm{eq}}}{\partial \boldsymbol{\varepsilon}} \boldsymbol{B} \ \mathrm{d}\Omega \tag{25}$$

$$\boldsymbol{K}^{\varepsilon\varepsilon} = \frac{\partial \boldsymbol{R}^\varepsilon}{\partial \bar{\varepsilon}_{\mathrm{eq}}} = \int_\Omega \left(\bar{\boldsymbol{N}}^T \bar{\boldsymbol{N}} + g l^2 \bar{\boldsymbol{B}}^T \bar{\boldsymbol{B}} + \bar{\boldsymbol{B}}^T l^2 \nabla \bar{\varepsilon}_{\mathrm{eq}} \frac{\mathrm{d}g}{\mathrm{d}\omega} \frac{\mathrm{d}\omega}{\kappa} \frac{\mathrm{d}\kappa}{\mathrm{d}\bar{\varepsilon}_{\mathrm{eq}}} \bar{\boldsymbol{N}} \right) \ \mathrm{d}\Omega. \tag{26}$$

The resulting asymmetric system of equations is solved with the LU decomposition of the MUMPS solver (Amestoy et al. 2001; Amestoy et al. 2006).

A line search algorithm is used to increase the robustness of the method. After solving the system, the solution $\Delta \boldsymbol{u} = (\Delta \underline{\boldsymbol{d}} \;\; \Delta \underline{\bar{\varepsilon}}_{\text{eq}})^T$ is applied with a factor η. Both conditions

$$\|\boldsymbol{R}(\boldsymbol{u} + \eta \Delta \boldsymbol{u})\| < \epsilon \tag{27}$$

$$\|\boldsymbol{R}(\boldsymbol{u})\| - \|\boldsymbol{R}(\boldsymbol{u} + \eta \Delta \boldsymbol{u})\| \geq \frac{1}{2}\eta \|\boldsymbol{R}(\boldsymbol{u})\| \tag{28}$$

must hold to accept the solution, where ϵ is a tolerance and $\|\cdot\|$ a residual norm. The first condition ensures a converged solution and the second one a quadratic convergence. If both conditions fail, η (initially $\eta = 1$) is reduced by a factor of 1/2 up to six times. If the conditions are still not fulfilled, the equilibrium for time $t + \Delta t$ is not reached. For a fixed Δt, this causes the whole time integration to fail. In an adaptive scheme, as shown Algorithm 1, the previous solution of time t is restored and a smaller Δt is chosen.

Algorithm 1: Adaptive backward Euler time stepping scheme

Global degrees of freedom $\boldsymbol{u}$
history variables $\boldsymbol{\kappa}$
initial time step Δt
while *time* $t < t_{end}$, *step* n **do**
  Increase load increment
  Solve for new state $\boldsymbol{u}_n, \boldsymbol{\kappa}_n$ within N Newton-Raphson iterations and a line search algorithm
  if $N < 3$ **then**
    $\Delta t = \min(1.5\Delta t, \Delta t_{\max})$
  end
  if *no convergence* **then**
    if $\Delta t < \Delta t_{\min}$ **then**
      Abort
    end
    restore $\boldsymbol{u}_{n-1}, \boldsymbol{\kappa}_{n-1}$
    $\Delta t = 0.5\Delta t$
    continue
  end
end

IMPL-EX TIME INTEGRATION

The implicit/explicit (IMPL-EX) scheme (Oliver et al. 2008) is a time integration scheme for nonlinear constitutive models. These nonlinearities often arise from internal history variables of the model and their evolution equations. Those variables store the state of the material, e.g. the plastic strains in a plasticity model, or in this case, the historic maximum of the nonlocal equivalent strains κ. By extrapolating those variables based on previously calculated values, the nonlinearities vanish. The resulting system is now linear, which leads to a robust solution procedure and increases the overall performance of the simulation.

Again, the pseudo time t is discretized into several time steps, Δt_n for the n-th step, and each step consists of three stages. The *explicit stage* performs an extrapolation of the history variables. In the present model, the history variable κ is driven by the nonlocal strain field. Its value is continuous in time and, because of the nonlocality, continuous in space. Thus, it is a reasonable choice for the extrapolation variable - in contrast to the damage variable ω that exhibits a jump in the derivative upon damage initiation at κ_0 (see Eq. (12)). The extrapolation for the time step $n+1$ reads

$$\tilde{\kappa}_{n+1} = \kappa_n + \frac{\Delta t_{n+1}}{\Delta t_n} \Delta \kappa_n \text{ with} \tag{29}$$

$$\Delta \kappa_n = \kappa_n - \kappa_{n-1}, \tag{30}$$

where $(\,\tilde{}\,)$ denotes the extrapolated values.

The second stage of the scheme is the solution of the global system of equations. The value of $\tilde{\kappa}_{n+1}$ is no longer unknown and replaces κ in Eqs. (20) to (26). Note that the derivative with respect to κ in Eq. (24) vanishes, resulting in $\boldsymbol{K}^{d\varepsilon} = \boldsymbol{0}$. Consequently, the system of equations in Eq. (22) can be solved separately in two steps. Firstly, the displacement degrees of freedom $\underline{\boldsymbol{d}}_{n+1}$ are solved via the linear equations

$$\boldsymbol{K}^{dd}(\underline{\boldsymbol{d}}_n, \tilde{\kappa}_{n+1}) \Delta \underline{\boldsymbol{d}}_{n+1} = -\boldsymbol{R}^d(\underline{\boldsymbol{d}}_n, \tilde{\kappa}_{n+1}). \tag{31}$$

Secondly, also Eq. (21) turns into a linear equation, because the displacements $\underline{\boldsymbol{d}}_{n+1}$ are now known and $g = g(\omega(\tilde{\kappa}_{n+1}))$, so $\mathrm{d}g/\mathrm{d}\kappa = 0$. It can be reformulated to directly obtain the new nonlocal equivalent strains with

$$\boldsymbol{R}^{\varepsilon} = \int_{\Omega} \left(\bar{\boldsymbol{N}}^T \bar{\boldsymbol{N}} + g l^2 \bar{\boldsymbol{B}}^T \bar{\boldsymbol{B}} \right) \mathrm{d}\Omega \; \underline{\bar{\boldsymbol{\varepsilon}}}_{\mathrm{eq},n+1} - \int_{\Omega} \bar{\boldsymbol{N}}^T \varepsilon_{\mathrm{eq}}(\underline{\boldsymbol{d}}_{n+1}) \; \mathrm{d}\Omega = \boldsymbol{0} \tag{32}$$

$$\boldsymbol{K}^{\varepsilon\varepsilon}_{\frac{\mathrm{d}}{\mathrm{d}\kappa}=0} \; \underline{\bar{\boldsymbol{\varepsilon}}}_{\mathrm{eq},n+1} = \int_{\Omega} \bar{\boldsymbol{N}}^T \varepsilon_{\mathrm{eq}}(\underline{\boldsymbol{d}}_{n+1}) \; \mathrm{d}\Omega. \tag{33}$$

For the case of a constant nonlocal interaction, $g \equiv 1$, the matrix $\boldsymbol{K}^{\varepsilon\varepsilon}_{\mathrm{d}/\mathrm{d}\kappa=0}$ is constant. Then, the solution can be sped up by applying a precalculated factorization of the matrix to the changing right hand sides.

In the third and final *implicit stage* of the algorithm, the nodal values $\underline{\boldsymbol{d}}_{n+1}$ and $\underline{\bar{\boldsymbol{\varepsilon}}}_{\mathrm{eq},n+1}$ are fixed and the conditions in Eq. (11) are evaluated to obtain and store the implicit values κ_{n+1}. The old extrapolated values $\tilde{\kappa}_{n+1}$ are no longer needed. A summary of the whole scheme is provided in Algorithm 2.

Algorithm 2: General IMPL-EX scheme

Global degrees of freedom $\boldsymbol{u}$
internal variables $\boldsymbol{\kappa}$
initial time steps $\Delta t_0 = \Delta t_1 = \Delta t$
while *time* $t < t_{end}$*, step* n **do**
  1. *explicit stage:* Extrapolation (˜) of the internal variables
     $\tilde{\boldsymbol{\kappa}}_{n+1} = \boldsymbol{\kappa}_n + \frac{\Delta t_{n+1}}{\Delta t_n}(\boldsymbol{\kappa}_n - \boldsymbol{\kappa}_{n-1})$
  2. Solve $\boldsymbol{R}(\boldsymbol{u}_{n+1}, \tilde{\boldsymbol{\kappa}}_{n+1})$ for $\boldsymbol{u}_{n+1}$, possibly separated
     Note that derivatives with respect to $\boldsymbol{\kappa}$ vanish.
  3. *implicit stage:* Evaluate the evolution equation Eq. (10)
     $\boldsymbol{\kappa}_{n+1} = \max(\bar{\boldsymbol{\varepsilon}}_{\mathrm{eq},n+1}, \boldsymbol{\kappa}_n)$

  if *adaptive time stepping* **then**
    Adjust Δt_{n+1} based on extrapolation error and Δt_n. See Section 5.
  else
    $\Delta t_{n+1} = \Delta t_n$
  end
end

The algorithm only requires the additional trivial implementation for the extrapolation of the history variables in Eq. (30). Other changes are significant simplifications compared to the backward Euler scheme.

First, backward Euler requires the calculation of the full algorithmic tangent matrix. In the IMPL-EX scheme, the algorithmic tangent stiffness in Eqs. (23) to (26) is reduced to the diagonal terms $\boldsymbol{K}^{dd}$ and $\boldsymbol{K}^{\varepsilon\varepsilon}$. This can save time when experimenting with new damage models or strain norms, because the derivatives $\partial\omega/\partial\kappa$ and $\partial\bar{\varepsilon}_{\text{eq}}/\partial\boldsymbol{\varepsilon}$ are not required. Especially the strain norms often include strain invariants or eigenvalues, where implementing the derivatives is error prone and time consuming.

Secondly, a Newton-Raphson algorithm has to be employed for the solution of the nonlinear system of equations in the backward Euler scheme, often coupled with a line search algorithm for additional stability. For IMPL-EX, the system of equations becomes linear and is solved only once per load increment. Therefore, a Newton-Raphson algorithm is not required. The system also becomes symmetric and the faster LDL^T decomposition is employed. The decoupling of the monolithic system into two smaller systems for $\boldsymbol{d}$ and $\bar{\varepsilon}_{\text{eq}}$ decreases the total solution time in a direct solver. Altogether, the computational effort for solving a single time step is greatly reduced.

Thirdly, a backward Euler requires small time steps in certain parts of the loading process to remain on the equilibrium path. Thus, a feasible implementation has to include an adaptive time stepping scheme. If a Newton-Raphson iteration fails to converge for a given time step, it is restarted with a smaller one. This requires restoring of nodal values and history variables of the last converged time step. In adaptive time stepping schemes for IMPL-EX (see next section), this is not required.

The extrapolation of the history variables in IMPL-EX defines a modified residual that approximates the equilibrium state, but does not exactly fulfill it. For a well-posed problem, decreasing the time step and decreasing the element sizes, the IMPL-EX scheme converges to the exact solution. However, for ill-posed problems such as problems with snap-back phenomena or bifurcation, an inexact solution will be obtained. In case of bifurcation problems, the scheme will decide to continue on one branch of the bifurcation, for snap-back phenomena it will jump over the snap back.

Within the IMPL-EX scheme, all hessian matrices are symmetric and positive definite (for damage $\omega > 0$, which is fulfilled by the damage law Eq. (12)). This is in contrast to the generally used backward Euler method. There, the ill-posedness of the problem results in convergence problems related to the numerical solution of the resulting system of equations. Even though the IMPL-EX scheme might not be able identify ill-posed problems, it often gives valuable insights into the failure mechanisms, e.g. the occurrence snap-backs. For some problems with bifurcation (e.g. a symmetric particle embedded in a matrix that cracks along that particle interface or extending this to mesoscale models with many particles), it is of interest to follow an arbitrary branch within the bifurcation problem.

The extrapolation of κ eliminates the nonlinearities in Eq. (20) corresponding to the nonlinear relation between stress and damage(κ). If the proposed algorithm is applied to problems with additional nonlinearities, a linear system can be obtained by defining these variables as internal variables and extrapolate them. One example is the monolithic solution of the system instead of the more efficient split into subsystems. In this case, the term $\boldsymbol{K}^{\varepsilon d}$ (Eq. (25)) still contains the nonlinear derivative of the strain norm ε_{eq} with respect to the strains. Other examples include stress-strain relations that distinguish between damage in compression and tension to model crack closure effects (Desmorat 2016).

ADAPTIVE IMPL-EX TIME STEPPING

The IMPL-EX scheme introduces an additional error, the extrapolation error of $\tilde{\kappa}$. This error is influenced by the time step Δt and smaller time steps will result in smaller extrapolation errors. Even though κ is continuously growing, the resulting stresses may not. They are calculated with the damage law in Eq. (12). At damage initiation ($\kappa = \kappa_0$), this function transitions from $\omega = 0$ to a very steep gradient. It is crucial to capture this event with a fine resolution to obtain a small error in the residual. However, there is no need for a high resolution in the elastic loading regime ($\kappa < \kappa_0$) or when the material is almost fully damaged ($\kappa \gg \kappa_0$). Increasing the time steps in these situations can save a significant amount of iterations.

The goal of the adaptive time stepping is to find a way of calculating the new time step Δt_{n+1} such that it keeps the extrapolation error bounded. For the present model, this means smaller time steps in the region of damage initiation and larger ones elsewhere. Two adaptive time stepping schemes for IMPL-EX are presented by (Oliver et al. 2008) and (Blanco et al. 2007). Both schemes find the new time step based on the maximal absolute extrapolation error of the internal variables. The derivation of similar error schemes for the present model is shown in Section 5. After that, two new classes of error control schemes are introduced, one based on the *relative* error of the internal variables in Section 5 and one based on the absolute error of the damage variable in Section 5. All presented schemes are summarized in Table 1.

Absolute error control

The absolute extrapolation error $e^{\text{extrapolation}}$ is limited to a certain fraction ξ of the material parameter κ_0

$$e^{\text{extrapolation}}_{n+1}(\boldsymbol{x}) = |\kappa_{n+1}(\boldsymbol{x}) - \tilde{\kappa}_{n+1}(\boldsymbol{x})| \le \xi\kappa_0 \quad \forall \boldsymbol{x} \in \Omega. \tag{34}$$

Taylor expansion of κ_{n+1} yields

$$\kappa_{n+1} = \kappa_n + \dot{\kappa}_n \Delta t_{n+1} + \frac{1}{2}\ddot{\kappa}_n \Delta t^2_{n+1} + \mathcal{O}(\Delta t^3_{n+1}) \tag{35}$$

and the approximation of the first time derivative $\dot{\kappa}_n \approx \Delta\kappa_n / \Delta t_n$ from the previous time step

$$\kappa_{n+1} \approx \underbrace{\kappa_n + \Delta\kappa_n \frac{\Delta t_{n+1}}{\Delta t_n}}_{\tilde{\kappa}_{n+1}} + \frac{1}{2}\ddot{\kappa}_n \Delta t^2_{n+1} \tag{36}$$

$$e^{\text{extrapolation}}_{n+1} \approx \frac{1}{2}|\ddot{\kappa}_n| \Delta t^2_{n+1} \tag{37}$$

eliminates $\tilde{\kappa}_{n+1}$ from Eq. (34). Approximating $\ddot{\kappa}_n$ and using Eq. (30) leads to

$$|\ddot{\kappa}_n| \approx \frac{|\dot{\kappa}_n - \dot{\kappa}_{n-1}|}{\Delta t_n} = \frac{1}{\Delta t_n^2}\left|\kappa_n - \kappa_{n-1} - \Delta\kappa_{n-1}\frac{\Delta t_n}{\Delta t_{n-1}}\right|$$
$$= \frac{1}{\Delta t_n^2}\left|\kappa_n - \tilde{\kappa}_n\right| = \frac{1}{\Delta t_n^2} e_n^{\text{extrapolation}}. \tag{38}$$

Inserted into Eq. (37), this relates the approximation of the extrapolation error at step $n+1$ to the known value $e_n^{\text{extrapolation}}$ of the previous time step. The new time step depends on the largest extrapolation error for all quadrature points and Eq. (34) now reads

$$\Delta t_{n+1} \leq \Delta t_n \min_{\boldsymbol{x}\in\Omega} \sqrt{\frac{2\xi\kappa_0}{|\kappa_n(\boldsymbol{x}) - \tilde{\kappa}_n(\boldsymbol{x})|}}\ . \tag{39}$$

As pointed out by (Oliver et al. 2008), limiting the time step growth with the acceleration factor $\eta = 1.3$ via $\Delta t_{n+1} \leq \eta\Delta t_n$ is beneficial. This also covers the case of a vanishing extrapolation error $e \approx 0$ since the resulting time step is limited. This case occurs in the elastic regime at the beginning of the simulations. Here, the automatic time stepping only depends on the initial time step Δt_0 that has to be chosen small enough so that the first time step remains within the elastic regime. This limitation with η is also applied for all further adaptive time stepping algorithms.

A different approach aims for limiting the absolute change of κ during one time step using the condition

$$e_{n+1}^{\text{increment}}(\boldsymbol{x}) = \tilde{\kappa}_{n+1}(\boldsymbol{x}) - \kappa_n(\boldsymbol{x})$$
$$= \Delta\kappa_n(\boldsymbol{x})\frac{\Delta t_{n+1}}{\Delta t_n} \leq \xi\kappa_0 \quad \forall\boldsymbol{x}\in\Omega \tag{40}$$

leading to the new time step

$$\Delta t_{n+1} \leq \Delta t_n \min_{\boldsymbol{x}\in\Omega} \frac{\xi\kappa_0}{(\kappa_n(\boldsymbol{x}) - \kappa_{n-1}(\boldsymbol{x}))}\ . \tag{41}$$

Note that this approach does not include the extrapolated values $\tilde{\kappa}$ in the calculation of the new time step.

Since both approaches relate the error value to the fixed value κ_0, they are referred to as *absolute error control*.

Relative error control

A new class of adaptive time stepping schemes is derived from the absolute error schemes by changing the reference from the constant value κ_0 to $\kappa_n(\boldsymbol{x})$. This leads to the definition of the relative extrapolation error

$$r_{n+1}^{\text{extrapolation}}(\boldsymbol{x}) = \frac{e_{n+1}^{\text{extrapolation}}(\boldsymbol{x})}{\kappa_n(\boldsymbol{x})} \leq \xi \quad \forall \boldsymbol{x} \in \Omega \tag{42}$$

and the new time step

$$\Delta t_{n+1} \leq \Delta t_n \min_{\boldsymbol{x} \in \Omega} \sqrt{\frac{2\xi\kappa_n(\boldsymbol{x})}{|\kappa_n(\boldsymbol{x}) - \tilde{\kappa}_n(\boldsymbol{x})|}}. \tag{43}$$

The condition for the incremental relative error now reads

$$r^{\text{increment}}(\boldsymbol{x}) = \frac{e_{n+1}^{\text{increment}}}{\kappa_n(\boldsymbol{x})} \leq \xi \quad \forall \boldsymbol{x} \in \Omega \tag{44}$$

and yields

$$\Delta t_{n+1} \leq \Delta t_n \min_{\boldsymbol{x} \in \Omega} \frac{\xi\kappa_n(\boldsymbol{x})}{\kappa_n(\boldsymbol{x}) - \kappa_{n-1}(\boldsymbol{x})}. \tag{45}$$

Error control based on the damage variable

The overall structural equilibrium is determined by the stresses. They are closely related to the damage variable ω. Based on this idea, another novel approach aims at defining the extrapolation error in terms of ω

$$|(1-\tilde{\omega})-(1-\omega)| = |\tilde{\omega}-\omega| < \xi. \tag{46}$$

Following the derivation of (Blanco et al. 2007), the condition

$$e^{\omega}_{n+1}(\boldsymbol{x}) = \tilde{\omega}_{n+1}(\boldsymbol{x}) - \omega_n(\boldsymbol{x}) < \xi \quad \forall \boldsymbol{x} \in \Omega \tag{47}$$

has to hold. The term $\tilde{\omega}_{n+1}$ is rewritten as

$$\tilde{\omega}_{n+1} = \omega(\tilde{\kappa}_{n+1}) = \omega\left(\kappa_n + \Delta\kappa_n \frac{\Delta t_{n+1}}{\Delta t_n}\right) \tag{48}$$

$$\approx \omega(\kappa_n) + \frac{\partial \omega(\kappa_n)}{\partial \kappa} \Delta\kappa_n \frac{\Delta t_{n+1}}{\Delta t_n}. \tag{49}$$

and the new time step is defined as

$$e^{\omega}_{n+1} \approx \frac{\partial \omega(\kappa_n)}{\partial \kappa} \Delta\kappa_n \frac{\Delta t_{n+1}}{\Delta t_n} \tag{50}$$

$$\Delta t_{n+1} \leq \Delta t_n \min_{\boldsymbol{x}\in\Omega} \frac{\xi}{\frac{\partial \omega(\kappa_n(\boldsymbol{x}))}{\partial \kappa} \Delta\kappa_n(\boldsymbol{x})} \tag{51}$$

This method additionally requires the evaluation of the derivative $\partial\omega/\partial\kappa$ for the current value κ_n. By definition in Eq. (12) the derivative vanishes for $\kappa \leq \kappa_0$. This case is covered by the η limitation of the time step, introduced in Section 5.

NUMERICAL EXAMPLES

Double notched tensile test

The setup and the material parameters of this experiment (shown in Fig. 1) are taken from (Peerlings et al. 1998). The specimen has a thickness of 50 mm and plane-stress conditions are assumed. The mesh consists of quadrilateral elements with an edge length of 1.25 mm. The damage law is visualized in Fig. 2 and the modified Mises equivalent strain norm from Eq. (16) is used. As in the reference implementation, a constant nonlocal interaction ($g(\omega) \equiv 1$) is used.

The displacements at the bottom of the specimen are fixed. The load is applied at the top using direct displacement control and is gradually increased up to the pseudo time $t = 1s$. The final damage distribution is show in Fig. 3. This experiment is now used to analyze the fixed and adaptive time stepping schemes introduced in the previous sections. The results are shown in Fig. 4, where the accuracy is measured by the global fracture energy G_f and the number of iterations indicates the performance.

Remark: The term iteration refers to Newton-Raphson iterations and corresponds to the number of direct solver calls. In this example, a single backward Euler iteration takes about 0.16 s, an IMPL-EX iteration about 0.08 s. Thus, a qualitative comparison in terms of computational time can be deduced by adding the factor 2 to the backward Euler simulations. The global fracture energy G_f is calculated by a trapezoidal integration of the load-displacement curve up to the boundary displacement $\Delta u = 0.1\,\text{mm}$. This is further explained in Appendix I.

A reference fracture energy $G_{f,\text{ref}}$ is obtained by a high resolution (6400 fixed time steps) backward Euler calculation.

The fixed time stepping schemes are compared first, IMPL-EX as ${}^{\text{IMPL-EX}}_{\text{fixed}}$ and backward Euler as ${}^{\text{backw. Euler}}_{\text{fixed}}$. The latter one requires a certain minimal time step, typically near the peak load, to find a converged solution. In this setup, the least accurate solution requires a time step $\Delta t = 1/1600\,\text{s}$ that corresponds to 3939 iterations. That means that the backward Euler time integration scheme cannot fulfill conditions Eqs. (27) to (28) with a significantly larger time step. The IMPL-EX scheme with a fixed time step cannot obtain the same accuracy with a comparable number of iterations. It is, however, capable to find a less accurate solution with far less iterations - for example only ≈ 250 iterations at $1\,\%$ error.

Each adaptive IMPL-EX scheme defines the variable ξ that controls the error threshold. A lower threshold leads to smaller time steps and, thus, to more iterations. These schemes are compared to each other and to an adaptive backward Euler simulation, marked at about 200 iterations with $^{\text{backw. Euler}}_{\text{adaptive}}$.

The $r^{\text{increment}}$ outperforms the other schemes for less than 1000 iterations. For a higher number of iterations, the e^{ω} scheme is the most accurate one. To understand the performance and accuracy differences, the behavior at the peak load of the load-displacement curve is analyzed next. The parameter ξ is chosen to result in about 100 iterations in each scheme and the corresponding load-displacement curves are plotted in Fig. 5. As in Fig. 4, $^{\text{backw. Euler}}_{\text{fixed}}$ marks a high resolution reference solution.

IMPL-EX with fixed time steps and the absolute error schemes miss the point of damage initiation and overestimate the peak load by $\approx 10\,\%$. The overshooting of the relative and damage based schemes is significantly smaller. The damage based scheme resolves the peak load more accurately whereas the relative incremental schemes continues closer to the reference equilibrium path in the post-peak region.

The value of the history parameter κ at the peak load is small ($= \kappa_0$) compared to the value in the damaged material ($\gtrapprox 25\kappa_0$ for $\omega > 0.99$). A small error $\Delta\kappa$ at peak load causes a much larger error in the resulting damage value (and the residual $\boldsymbol{R}$) than the same $\Delta\kappa$ in the almost completely damaged material. The relative error schemes and the one using ω directly exploit this fact. This results in a time step distribution with short time steps in the region of the peak load and larger time steps towards the end of the simulation. Thus, they generally perform better than their absolute counterparts - and the fixed stepping. The adaptive schemes $r^{\text{increment}}$ and e^{ω} perform best. Thus, they are further analyzed in the following examples to find the most suitable scheme. IMPL-EX with fixed time steps is also considered further as a simple alternative to the adaptive, error controlled time stepping.

Two-dimensional compression test

The setup of the next example is shown in Fig. 6. It is simulated under plane stress conditions and 120×120 quadrilateral elements with quadratic interpolation for $\boldsymbol{d}$ and $\bar{\varepsilon}_{\text{eq}}$. It is taken from (Poh and Sun 2017), where it is used to demonstrate the correct failure pattern of the decreasing nonlocal interaction model (g from Eq. (3)). In this setup, a mode II failure is expected with an inclined shear band starting from the defect region (Fig. 7), whereas the constant interaction models with a constant length scale parameter l show a horizontal localization.

The comparison of the backward Euler time integration with the IMPL-EX time integration is shown in Fig. 8. To evaluate the computational effort related to each calculation, a simulation time is measured and shown in the legend. The time spent in the solver (here MUMPS(Amestoy et al. 2001; Amestoy et al. 2006)) is used, because this time usually dominates the total simulation time, but does not depend on implementation details of the used finite element tool.

The fixed time stepping schemes in Fig. 8a are compared first. Similar results as in Section 6 are observable. The backward Euler simulation requires a certain minimal time step to find the equilibrium solution. In this case, this time step lays between $\Delta t = 0.0006s$ (failed, not shown in the plot) and $\Delta t = 0.0005s$. The IMPL-EX simulations find a good agreement with far less iterations. For $\Delta t = 0.005$, the curve overestimates the peak load and deviates slightly deviates from the equilibrium path. For smaller IMPL-EX time steps, the load-displacement curve is in good agreement with the backward Euler solution, for a fraction of the solver time.

Figure 8b compares the damage based time stepping from Section 5 to the adaptive backward Euler simulation. For all values of ξ, the peak load is well resolved, but the forces on the softening branch of the load-displacement curve are overestimated. Smaller values of ξ do fix this problem. Then, however, the computational effort is similar or higher compared to the fixed time stepping. However, these adaptive methods have the advantage that the time step does not have to be prescribed a priori. The time step concentration over the whole load-displacement curve is indicated by the vertical marks. The backward Euler simulation shows a higher concentration around the peak load, but the softening branch is also resolved. The damage based error control limits the growth of the damage variable. On damage initiation, the derivative $\mathrm{d}\omega/\mathrm{d}\kappa$ is very steep and the resulting time steps are very small. As κ grows further, the derivative rapidly goes towards zero and causes large time steps, not only in the fully localized state, but already in the softening branch. This is in agreement with the mark distribution of Fig. 8b.

Figure 8c shows the relative incremental error scheme in comparison to adaptive backward Euler. Apart from a slight overestimation of the peak load, the solution for $\xi = 0.1$ is hard to distinguish from the backward Euler simulation. Compared to the latter one, a solver time speedup of about 6 is reached. Due to the matrix sparsity and size of the system, a performance difference is more pronounced in a larger, three dimensional simulation and will be discussed based on the next example.

Three-dimensional compression test

The aim of this experiment is to show the performance aspect of the IMPL-EX scheme compared to a backward Euler integration. The mesoscale geometry of the $40\,\mathrm{mm} \times 40\,\mathrm{mm} \times 40\,\mathrm{mm}$ specimen is randomly generated (Titscher and Unger 2015) from a B16 grading curve (defined in DIN 1045-2) and 60 % aggregate volume fraction. Aggregates smaller than 8 mm are assumed to be represented by the matrix material and were not resolved explicitly.

The material models used in this experiment are taken from (Unger and Eckardt 2011) and are shown in Table 2. Tetrahedral elements are used for the matrix material and the aggregates. The interfaces are represented by pentahedral (wedge) elements and a regularized local damage model. The continuum strong discontinuity approach (CSDA) as introduced by (Oliver et al. 2002) has been applied to model the interfacial transition zone (ITZ) using very thin, regularized continuum elements. The ITZ is a very thin layer between concrete aggregates and the mortar matrix that is weaker than the surrounding material. This allows handling the interface elements in the same stress-strain framework as the bulk material.

In contrast to damage zones within the matrix material, the damage path in the ITZ is known a priori and CSDA elements with the local damage model

$$\boldsymbol{\sigma} = (1 - \omega(\kappa))\, \boldsymbol{C} : \boldsymbol{\varepsilon} \text{ with} \tag{52}$$

$$\dot{\kappa} \geq 0, \quad \varepsilon_{\text{eq}} - \kappa \leq 0, \quad \dot{\kappa}(\varepsilon_{\text{eq}} - \kappa) = 0 \tag{53}$$

are employed. In contrast to Eq. (10), the history variables κ are driven by the *local* equivalent strains ε_{eq}, defined in Eq. (16). The full tangent in the backward Euler scheme

$$\left(\frac{\partial \boldsymbol{\sigma}}{\partial \boldsymbol{\varepsilon}}\right)_{\text{backw. Euler}} = (1 - \omega(\kappa))\boldsymbol{C} - \boldsymbol{C} : \boldsymbol{\varepsilon} \frac{\partial \omega}{\partial \kappa} \frac{\partial \kappa}{\partial \varepsilon_{\text{eq}}} \frac{\partial \varepsilon_{\text{eq}}}{\partial \boldsymbol{\varepsilon}} \tag{54}$$

includes a nonlinear second term that can lead to an ill-conditioned system (Jirásek 2007). For the IMPL-EX adaptation, similar to the one of the gradient enhanced damage model, the system is solved with the extrapolated values $\tilde{\kappa}$ instead of κ. Thus, the corresponding secant tangent

$$\left(\frac{\partial \boldsymbol{\sigma}}{\partial \boldsymbol{\varepsilon}}\right)_{\text{IMPL-EX}} = (1 - \omega(\tilde{\kappa}))\boldsymbol{C} \tag{55}$$

used in the solution procedure of IMPL-EX remains positive definite.

The displacement field $\boldsymbol{d}$ is discretized according to Eq. (17) with the same interpolation order as for the gradient damage model.

The damage law from Eq. (12) is used and the fracture energy parameter g_f is regularized with the element thickness t via

$$g_f = \frac{G_f}{t}. \tag{56}$$

Obtaining the fracture energy parameter g_f for the nonlocal matrix material requires a calibration. This is done in a one dimensional tensile test with a similar setup as in Appendix I. Displacement boundary conditions are applied at the top and bottom surface. Movement in the horizontal directions is suppressed to model the static friction between the specimen and the testing machine. In horizontal direction, the bottom is fixed and direct displacement control is applied to all nodes of the top surface. The other surfaces are stress-free. All fields (geometry, $\boldsymbol{d}$ and $\bar{\varepsilon}_{\mathrm{eq}}$) are interpolated with quadratic shape functions. The average element length as well as the nonlocal length parameter l is chosen to be 2 mm. The resulting mesh has $\approx 5 \times 10^4$ elements and $\approx 3.3 \times 10^5$ degrees of freedom.

The resulting load-displacement curves for different time integration schemes are shown in Fig. 11. There is nearly no visible difference between the IMPL-EX solution with 400 fixed time steps and the adaptive backward Euler reference solution. Due to the rather long solution time of the latter one, we do not provide a backward Euler solution with a fixed time step. The IMPL-EX calculation with 200 time steps suffers from a small oscillation near the peak load and continues very close to the equilibrium path. Compared to the backward Euler simulation, this results in a computational speedup of ≈ 11. Significant overshooting to 110 % of the peak load is observable for IMPL-EX with 50 fixed time steps. The adaptive time stepping scheme with $\xi = 0.15$ corresponds to 57 time steps and resolves the peak load correctly. Its accuracy is comparable to IMPL-EX with 200 fixed time steps. Thus, the speedup compared to the adaptive backward Euler solution increases to ≈ 40. Another adaptive simulation with $\xi = 0.25$ is shown. It corresponds to 44 time steps and resolves the peak load with an error of ≈ 5 %. In the post-peak behavior it deviates from the equilibrium path, which introduces an additional error in the global fracture energy.

The differences in the wall time required to perform the simulations, has two main reasons. First, the number of iterations itself. The backward Euler scheme requires 259 time steps, with multiple iterations within each step due to the nonlinearity. Additionally, some time steps do not reach the desired tolerance within the maximum number of iterations and require a restart with a reduced time step. This results in 1100 total solutions of the global system of equations. Second, the time per iteration differs. In the backward Euler scheme, the asymmetric sparse system Eq. (22) is solved for both the displacements *and* the nonlocal equivalent strains, resulting in $\approx 108\,\mathrm{s}$ per solve. The IMPL-EX scheme requires $\approx 53\,\mathrm{s}$ per iteration, since the system is split. The solution of Eq. (33) is sped up by using a factorization that is calculated only once at the beginning of the simulation. The remaining Eq. (31) yields a linear, symmetric system containing only the displacement degrees of freedom.

CONCLUSIONS

The IMPL-EX integration of the implicit gradient enhanced damage model is presented as an alternative to a classic, backward Euler time integration. Its implementation is less invasive and mainly requires the extrapolation of the history variables. This decouples the system of equations and provides various numerical benefits. The backward Euler algorithm requires the full algorithmic stiffness and the resulting monolithic system is nonlinear and asymmetric. The decoupling allows a subsequent solution of each subsystem, in which one tangent is linear and symmetric and the second one, for the classic model with constant nonlocal interaction, is constant. Additionally, off-diagonal terms in the algorithmic stiffness matrix are no longer required and only the block-diagonal matrix entries have to be computed/implemented.

A significant speedup can be achieved for simulations involving complex geometries, like concrete on the mesoscale, where backward Euler schemes exhibit instabilities. There is a certain minimal time step for the backward Euler scheme which constrains the run time of the simulation. By accepting a loss in accuracy, the IMPL-EX scheme can find solutions with an arbitrary number of iterations. The actual speedup, however, strongly depends on the problem. In a three-dimensional compression test, a reasonable approximation of an adaptive backward Euler solution is obtained with equidistant IMPL-EX time steps and a speedup of ≈ 11.

IMPL-EX extrapolation errors during the damage initiation have a larger influence than the same errors in a nearly fully damaged material. Since smaller time steps lead to smaller errors, it is beneficial to concentrate the time steps around the point of damage initiation. This is achieved by using adaptive time stepping algorithms. The performance of three different classes of algorithms is assessed. The scheme that limits the relative error of the history variables performs best. It is capable of reducing the number of iterations while maintaining the accuracy. In the the three-dimensional compression test mentioned above, a significant speedup (≈ 40) is obtained.

ACKNOWLEDGMENT

The research was supported by the Federal Institute for Materials Research and Testing, Berlin, Germany and by the German Research Foundation (DFG) under project Un224/7-1. Additionally, the research leading to these results has received funding from the European Research Council under the European Union's Seventh Framework Programme (FP/2007-2013) / ERC Grant Agreement n. 320815 (ERC Advanced Grant Project "Advanced tools for computational design of engineering materials" COMP-DES-MAT).

References

Amestoy, P. R., Duff, I. S., Koster, J., and L'Excellent, J.-Y. (2001). "A fully asynchronous multifrontal solver using distributed dynamic scheduling." *SIAM Journal on Matrix Analysis and Applications*, 23(1), 15–41.

Amestoy, P. R., Guermouche, A., L'Excellent, J.-Y., and Pralet, S. (2006). "Hybrid scheduling for the parallel solution of linear systems." *Parallel Computing*, 32(2), 136–156.

Bažant, Z. P. and Belytschko, T. B. (1985). "Wave propagation in a strain-softening bar: exact solution." *Journal of Engineering Mechanics*, 111(3), 381–389.

Bažant, Z. P., Belytschko, T. B., and Chang, T.-P. (1984). "Continuum theory for strain-softening." *Journal of Engineering Mechanics*, 110(12), 1666–1692.

Bažant, Z. P. and Jirásek, M. (2002). "Nonlocal integral formulations of plasticity and damage: survey of progress." *Journal of Engineering Mechanics*, 128(11), 1119–1149.

Bazant, Z. P. and Pijaudier-Cabot, G. (1988). "Nonlocal continuum damage, localization instability and convergence." *Journal of applied mechanics*, 55(2), 287–293.

Blanco, S., Oliver, J., and Huespe, A. (2007). "Contribuciones a la simulación numérica del fallo material en medios tridimensionales mediante la metodología de discontinuidades fuertes de continuo." Ph.D. thesis, Universitat Politécnica de Catalunya, Carol, I. and Bazant, Z. P. (1997). "Damage and plasticity in microplane theory." *International Journal of Solids and Structures*, 34(29), 3807–3835.

Carol, I., Prat, P. C., and López, C. M. (1997). "Normal/shear cracking model: application to discrete crack analysis." *Journal of engineering mechanics*, 123(8), 765–773.

Cazes, F., Meschke, G., and Zhou, M.-M. (2016). "Strong discontinuity approaches: An algorithm for robust performance and comparative assessment of accuracy." *International Journal of Solids and Structures*, 96, 355–379.

De Vree, J., Brekelmans, W., and Van Gils, M. (1995). "Comparison of nonlocal approaches in continuum damage mechanics." *Computers & Structures*, 55(4), 581–588.

Desmorat, R. (2016). "Anisotropic damage modeling of concrete materials." *International Journal of Damage Mechanics*, 25(6), 818–852.

Graça-e Costa, R., Alfaiate, J., Dias-da Costa, D., and Sluys, L. J. (2012). "A non-iterative approach for the modelling of quasi-brittle materials." *International Journal of Fracture*, 178(1), 281–298.

Jirásek, M. (2007). "Mathematical analysis of strain localization." *Revue européenne de génie civil*, 11(7-8), 977–991.

Jirásek, M. and Zimmermann, T. (1998). "Rotating crack model with transition to scalar damage." *Journal of engineering mechanics*, 124(3), 277–284.

Mazars, J. and Pijaudier-Cabot, G. (1989). "Continuum damage theory - application to concrete." *Journal of Engineering Mechanics*, 115(2), 345–365.

Oliver, J. (1989). "A consistent characteristic length for smeared cracking models." *International Journal for Numerical Methods in Engineering*, 28(2), 461–474.

Oliver, J., Cervera, M., Oller, S., and Lubliner, J. (1990). "Isotropic damage models and smeared crack analysis of concrete." *Second international conference on computer aided analysis and design of concrete structures*, Vol. 2, 945–958.

Oliver, J., Huespe, A., Blanco, S., and Linero, D. (2006). "Stability and robustness issues in numerical modeling of material failure with the strong discontinuity approach." *Computer*

Methods in Applied Mechanics and Engineering, 195(52), 7093–7114.

Oliver, J., Huespe, A., and Cante, J. (2008). "An implicit/explicit integration scheme to increase computability of non-linear material and contact/friction problems." *Computer Methods in Applied Mechanics and Engineering*, 197(21), 1865–1889.

Oliver, J., Huespe, A., Pulido, M., and Chaves, E. (2002). "From continuum mechanics to fracture mechanics: the strong discontinuity approach." *Engineering Fracture Mechanics*, 69(2), 113–136.

Peerlings, R., De Borst, R., Brekelmans, W., and Geers, M. (1998). "Gradient-enhanced damage modelling of concrete fracture." *Mechanics of Cohesive-frictional Materials*, 3(4), 323–342.

Peerlings, R., Geers, M., De Borst, R., and Brekelmans, W. (2001). "A critical comparison of nonlocal and gradient-enhanced softening continua." *International Journal of solids and Structures*, 38(44), 7723–7746.

Peerlings, R., Massart, T., and Geers, M. (2004). "A thermodynamically motivated implicit gradient damage framework and its application to brick masonry cracking." *Computer methods in applied mechanics and engineering*, 193(30-32), 3403–3417.

Peerlings, R. H. J., De Borst, R., Brekelmans, W. A. M., and De Vree, J. H. P. (1996). "Gradient enhanced damage for quasi-brittle materials." *International Journal for Numerical Methods in Engineering*, 39(19), 3391–3403.

Pham, K., Amor, H., Marigo, J.-J., and Maurini, C. (2011). "Gradient damage models and their use to approximate brittle fracture." *International Journal of Damage Mechanics*, 20(4), 618–652.

Pijaudier-Cabot, G. and Bažant, Z. P. (1987). "Nonlocal damage theory." *Journal of engineering mechanics*, 113(10), 1512–1533.

Poh, L. H. and Sun, G. (2017). "Localizing gradient damage model with decreasing interactions." *International Journal for Numerical Methods in Engineering*, 110(6), 503–522.

Rots, J., Nauta, P., Kuster, G., and Blaauwendraad, J. (1985). "Smeared crack approach and fracture localization in concrete." *Report no.*, Delft University of Technology.

Rots, J. G., Belletti, B., and Invernizzi, S. (2008). "Robust modeling of rc structures with an "event-by-event" strategy." *Engineering Fracture Mechanics*, 75(3), 590 – 614 International Conference of Crack Paths.

Simone, A., Askes, H., Peerlings, R., and Sluys, L. (2003). "Interpolation requirements for implicit gradient-enhanced continuum damage models." *International Journal for Numerical Methods in Biomedical Engineering*, 19(7), 563–572.

Titscher, T. and Unger, J. F. (2015). "Application of molecular dynamics simulations for the generation of dense concrete mesoscale geometries." *Computers & Structures*, 158, 274 – 284.

Triantafyllidis, N. and Aifantis, E. C. (1986). "A gradient approach to localization of deformation. i. hyperelastic materials." *Journal of Elasticity*, 16(3), 225–237.

Unger, J. F. and Eckardt, S. (2011). "Multiscale modeling of concrete." *Archives of Computational Methods in Engineering*, 18(3), 341.

Appendix I. ANALYSIS OF THE INTERPOLATION ORDER

As stated by (Simone et al. 2003), the Babuska-Brezzi condition does not apply for the discretized gradient enhanced continuum damage model. The interpolation orders for the displacement field and the nonlocal equivalent strain field do not need to be related and any interpolation can be employed.

Figure 12a shows the convergence analysis of a one-dimensional specimen of length L. The boundary $x = 0$ is fixed and the boundary condition $u(x = L) = \Delta u$ is applied in 10^4 equidistant load steps. An imperfection is imposed with a predamaged zone by setting the initial value $\kappa = 3\kappa_0$ in 2 % of the elements. The numerical integration uses five Gauss-Legendre integration points for all interpolation orders. The global fracture energy is chosen as a measure of the accuracy and is obtained by integrating (trapezoidal rule) the load-displacement curve

$$G_f = \frac{1}{A}\int F(u)\mathrm{d}u - \underbrace{L_\mathrm{E}\int_0^{3\kappa} \sigma(\kappa)\mathrm{d}\kappa}_{\text{pre-damage}} \ . \tag{57}$$

The reference solution $G_{f,\mathrm{ref}}$ is obtained from a simulation with 4000 elements and quartic interpolation for both fields, corresponding to 16000 DOFs.

The analysis for the double notched specimen from Section 6 is shown in Fig. 12b. The element size L_E is chosen as fractions of the notch geometry of 5 mm and the reference solution $G_{f,\mathrm{ref}}$ is obtained from a quadratic-quadratic interpolation with $L_E = 5\,\mathrm{mm}/24$.

The numerical cost of a backward Euler integration scheme is dominated by the solution of the global system of equations, which itself depends on the number of degrees of freedom (DOFs). Thus, the results in Fig. 12 do not represent a convergence analysis, but an analysis of the computational cost. The slope of the curves is influenced by the lowest interpolation order. The error for a given number of DOFs is *slightly* lower, if the displacement field is interpolated one order higher. However, if the higher order interpolation is available, it is highly beneficial to also use it for the nonlocal equivalent strain field, since it increases the overall order of the method.

Note that equal interpolation orders for both fields lead to jumps in the stress field, e.g. for the linear-linear case: Linear displacements result in constant strains. The stresses are calculated via the damage ω which depends on the nonlocal equivalent strain field $\omega(\kappa(\bar{\varepsilon}_{\mathrm{eq}}))$. Since they are allowed to change linearly, constant strains can lead to non constant stresses. This is a post-processing problem and can be solved by e.g. a smoothing of the stresses (Simone et al. 2003).

List of Tables

Table 1. Overview of the adaptive time stepping schemes

abbreviation	time step $\Delta t \leq \Delta t_n \min\limits_{\boldsymbol{x}\in\Omega} \dots$
$e^{\text{extrapolation}}$ Section 5	$\sqrt{\dfrac{2\xi\kappa_0}{\lvert\kappa_n(\boldsymbol{x}) - \tilde{\kappa}_n(\boldsymbol{x})\rvert}}$
$r^{\text{extrapolation}}$ Section 5	$\sqrt{\dfrac{2\xi\kappa_n(\boldsymbol{x})}{\lvert\kappa_n(\boldsymbol{x}) - \tilde{\kappa}_n(\boldsymbol{x})\rvert}}$
$e^{\text{increment}}$ Section 5	$\dfrac{\xi\kappa_0}{(\kappa_n(\boldsymbol{x}) - \kappa_{n-1}(\boldsymbol{x}))}$
$r^{\text{increment}}$ Section 5	$\dfrac{\xi\kappa_n(\boldsymbol{x})}{\kappa_n(\boldsymbol{x}) - \kappa_{n-1}(\boldsymbol{x})}$
e^{ω} Section 5	$\dfrac{\xi}{\frac{\partial\omega(\kappa_n(\boldsymbol{x}))}{\partial\kappa}\left(\kappa_n(\boldsymbol{x}) - \kappa_{n-1}(\boldsymbol{x})\right)}$

Table 2. Material parameters for the three-dimensional compression test.

Parameter	Unit	Matrix	Interface	Aggregate
Young's modulus E	[MPa]	26738	26738	$2 \cdot 26738$
Poisson's ratio ν		0.18	0.18	0.18
Strength				
tensile f_t	[MPa]	3.4	$F \cdot 3.4$	–
compressive f_c	[MPa]	34	$F \cdot 34$	–
Fracture energy				
global G_f	[N/mm]	0.12	$F \cdot 0.12$	–
local g_f	[MPa]	0.0216	$\frac{F}{t} \cdot 0.12$	–
Nonlocal parameter l	[mm]	2	–	–
Nonlocal interaction g		$\equiv 1$	–	–
Interface thickness t	[mm]	–	0.5	–
Interface reduction F		–	0.75	–

List of Figures

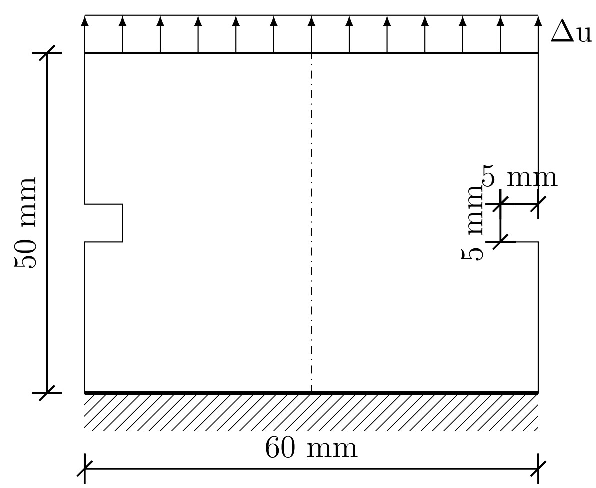

Fig. 1. Setup of the double-notched tensile test.

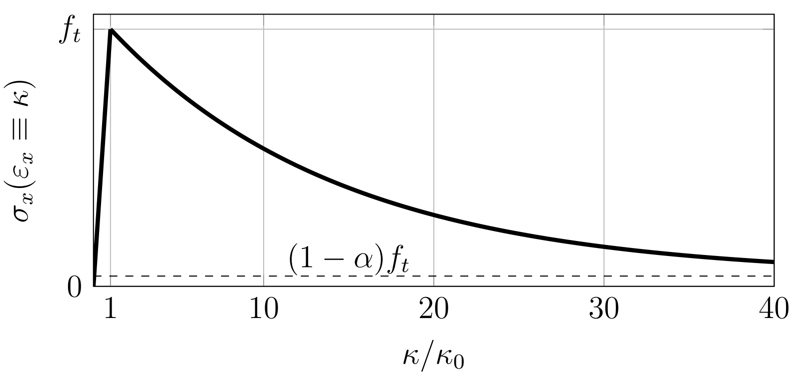

Fig. 2. One-dimensional stress-strain relation for the exponential damage law (Eq. (12)) and the material parameters from Fig. 1.

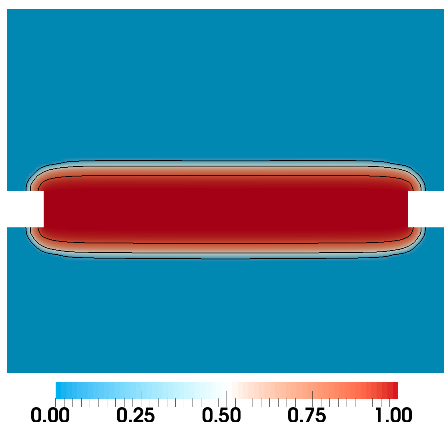

Fig. 3. The final damage distribution of the double-notched tensile test is shown as a contour plot. The iso-damage lines correspond to $\omega = [0.1, 0.5, 0.9]$ from outside to inside.

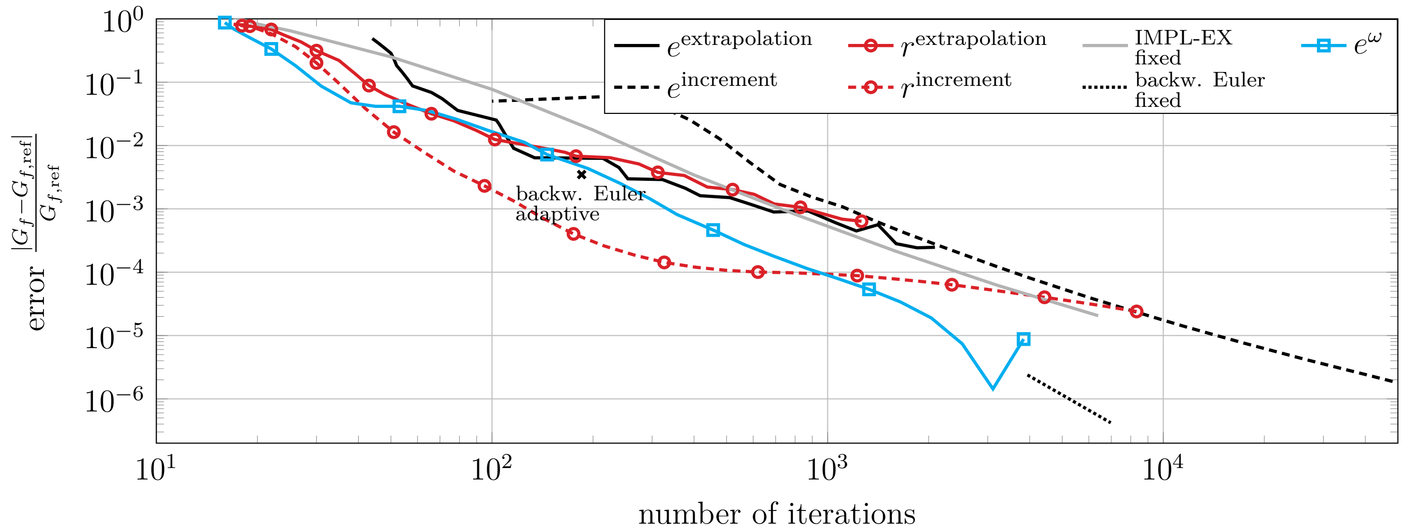

Fig. 4. Convergence analysis of the adaptive time stepping schemes for the double-notched tensile test.

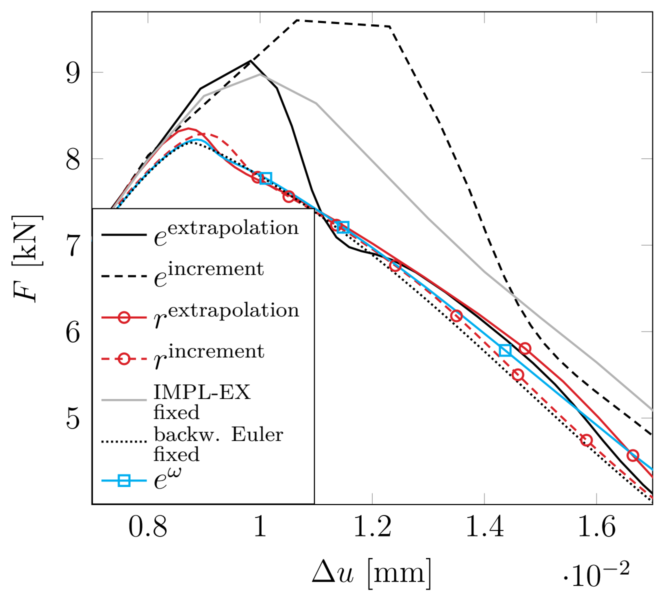

Fig. 5. Load-displacement curves for double notched specimen. All schemes (except the reference $^{\text{backw. Euler}}_{\text{fixed}}$) were adjusted to about 100 iterations.

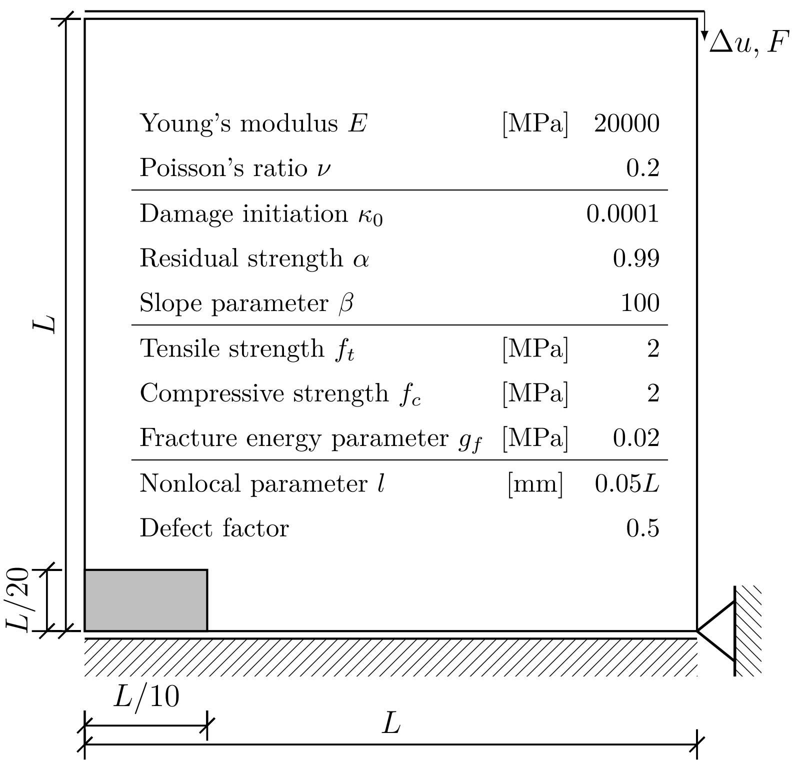

Young's modulus E	[MPa]	20000
Poisson's ratio ν		0.2
Damage initiation κ_0		0.0001
Residual strength α		0.99
Slope parameter β		100
Tensile strength f_t	[MPa]	2
Compressive strength f_c	[MPa]	2
Fracture energy parameter g_f	[MPa]	0.02
Nonlocal parameter l	[mm]	$0.05L$
Defect factor		0.5

Fig. 6. Setup of the two dimensional compression test. The gray defect region has a reduced damage initiation threshold of $\kappa_{0,\text{defect}} = 0.5\kappa_0$.

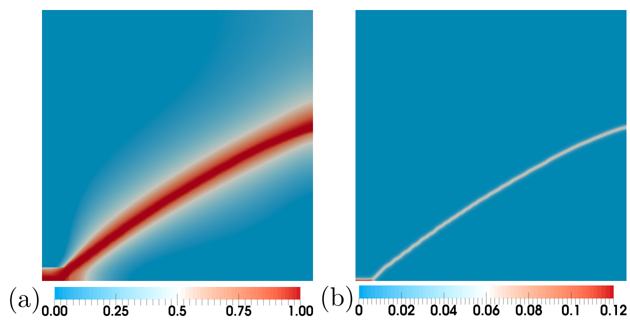

Fig. 7. Plots of the damage field ω (a) and the nonlocal equivalent strain field $\bar{\varepsilon}_{\mathrm{eq}}$ (b) of the two dimensional compression test.

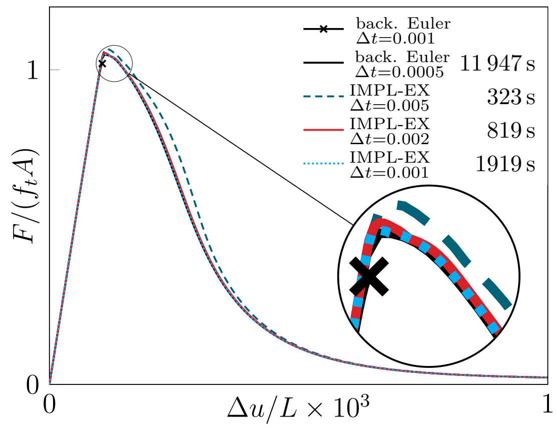

(a) Fixed time stepping.

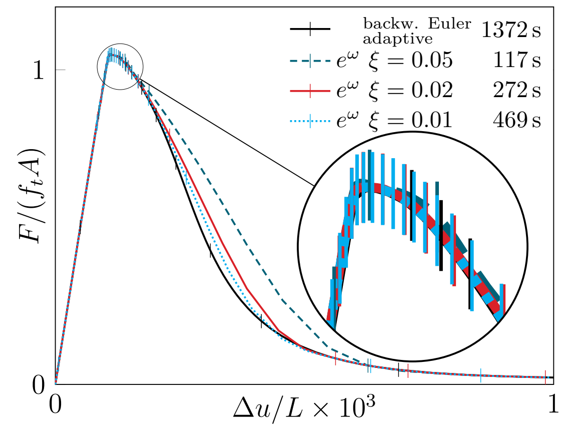

(b) Adaptive time stepping e^{ω} compared to adaptive backward Euler.

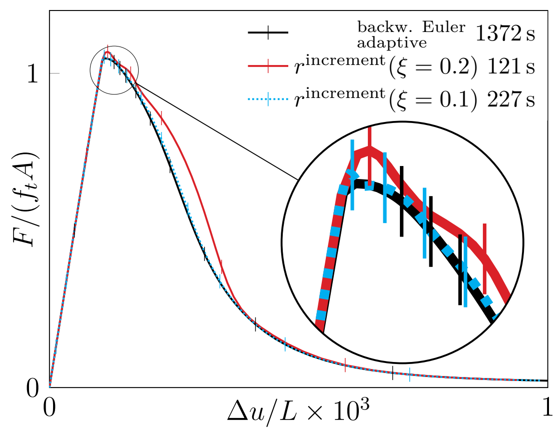

(c) Adaptive time stepping $r^{\text{increment}}$ compared to adaptive backward Euler.

Fig. 8. Load-displacement curves for the two dimensional compression test. The performance and accuracy of the backward Euler time integration is compared to the IMPL-EX time integration. Vertical marks indicate every 10th time step in the adaptive schemes to indicate the evolution of the time step.

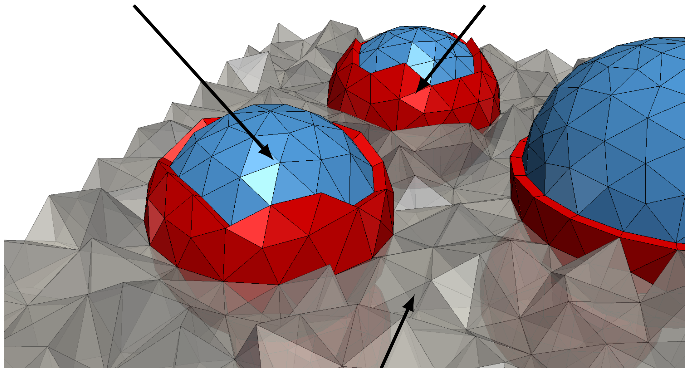

Fig. 9. Visualization of the mesoscale geometry and the used material models in the three-dimensional compression test.

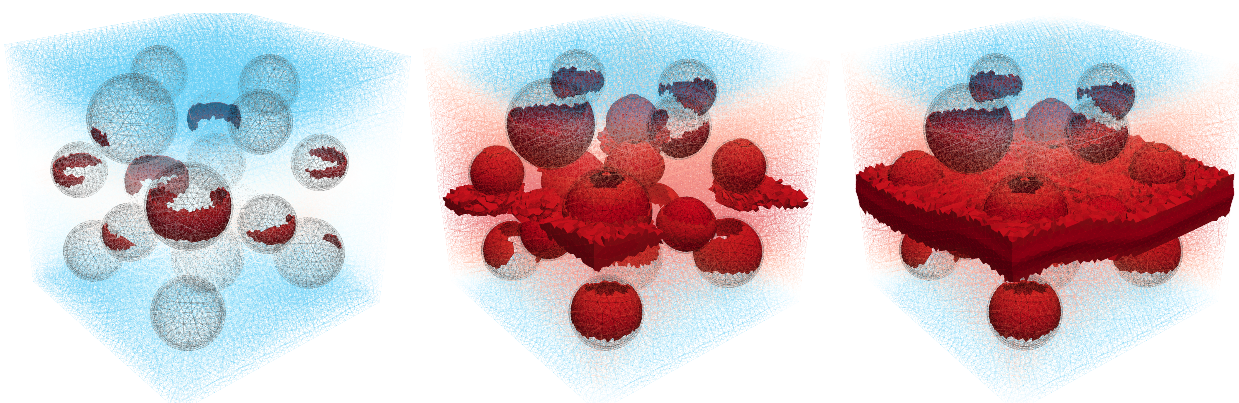

(a) $F = F_{\max}$ (b) $F = 0.6F_{\max}$ (c) $F = 0.25F_{\max}$

Fig. 10. Damage plot of the adaptive backward Euler solution at different loading states after the post-peak. Elements with damage $\omega > 0.99$ are shown as solid elements, others as wireframe.

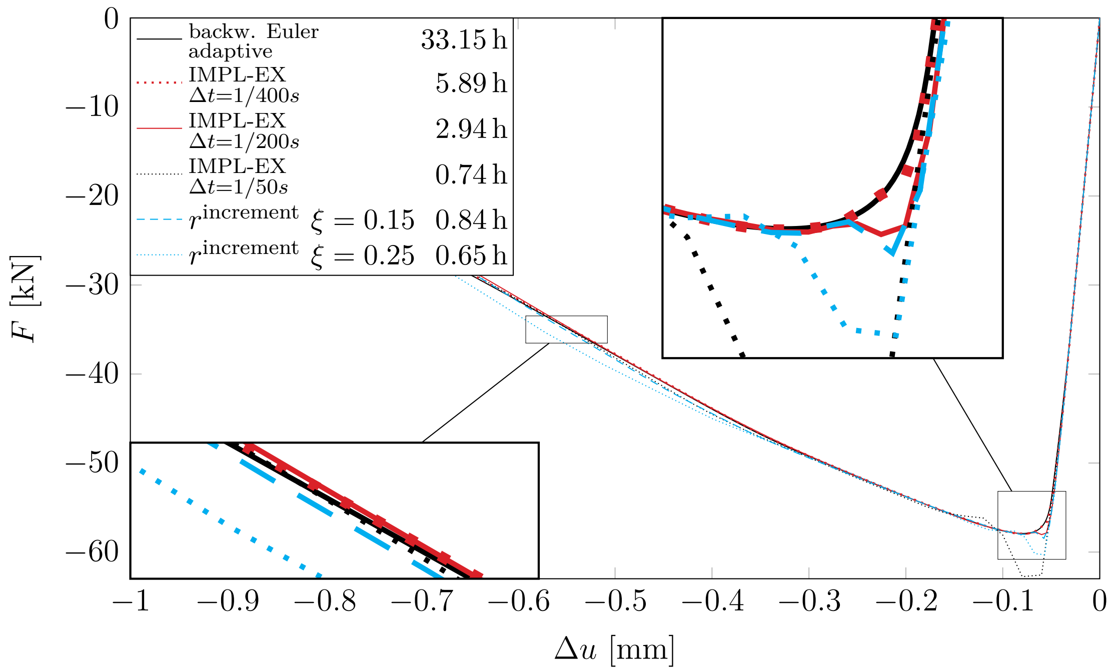

Fig. 11. Load-displacement curves for the three-dimensional compression test. The legend shows the solver time.

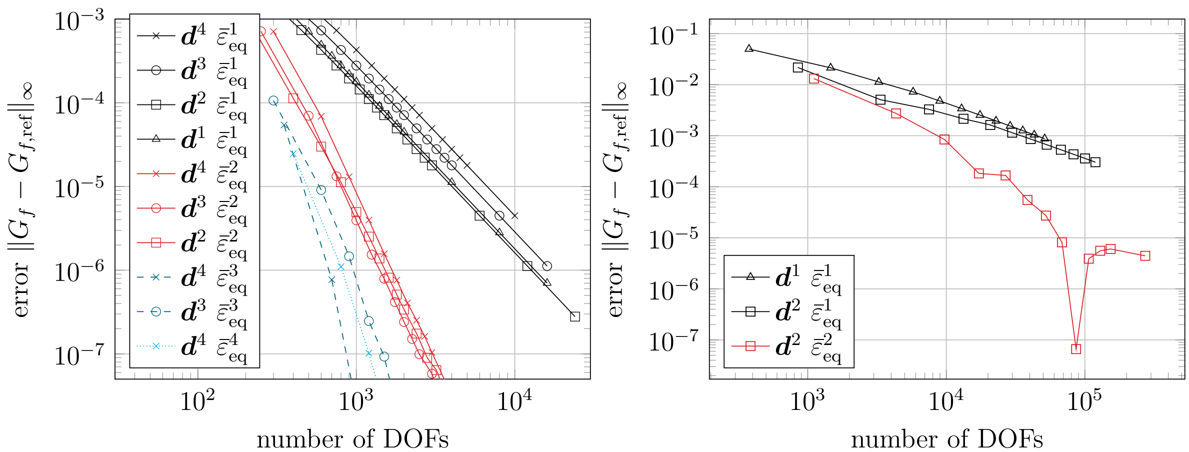

(a) 1D truss

(b) 2D double notch

Fig. 12. Analysis of the computational cost of different combinations of interpolation orders and element sizes (expressed as degrees of freedom (DOF)). The exponent in the legend shows the interpolation order for the displacement field $\boldsymbol{d}$ and the nonlocal equivalent strain field $\bar{\varepsilon}_{\mathrm{eq}}$.